The Astrophysical Journal, 939:39 (13pp), 2022 November 1 https://doi.org/10.3847/1538-4357/ac937c

GRB 110213A: A Study of Afterglow Electromagnetic Cascade Radiation

Xiang-Gao Wang[1,2], Yuan-Zhuo Chen[1,2], Xiao-Li Huang[3], Liang-Jun Chen[1,2], WeiKang Zheng[4], Valerio D'Elia[5,6], Massimiliano De Pasquale[7], Alexei S. Pozanenko[8,9,10], Li-Ping Xin[11], Giulia Stratta[12,13,14], Tilan Ukwatta[15], Carl Akerlof[16], Jin-Jun Geng[17], Xu-Hui Han[11], Veli-Pekka Hentunen[18], E. V. Klunko[19], N. Paul M. Kuin[20], Markku Nissinen[18], W. Rujopakarn[21], V. V. Rumyantsev[22], E. S. Rykoff[23], Tuomo Salmi[18], B. E. Schaefer[24], A. A. Volnova[25], Xue-Feng Wu[26], Jian-Yan Wei[11], En-Wei Liang[1,2], Bing Zhang[27,28], and Alexei V. Filippenko[4]

[1] Guangxi Key Laboratory for Relativistic Astrophysics, School of Physical Science and Technology, Guangxi University, Nanning, 530004, People's Republic of China; wangxg@gxu.edu.cn, lew@gxu.edu.cn
[2] GXU-NAOC Center for Astrophysics and Space Sciences, Nanning, 530004, People's Republic of China
[3] School of Physics and Electronic Science, Guizhou Normal University, Guiyang, 550025, People's Republic of China; xiaoli.huang@gznu.edu.cn
[4] Department of Astronomy, University of California, Berkeley, CA 94720-3411, USA; weikang@berkeley.edu
[5] ASI-Space Science Data Centre, Via del Politecnico snc I-00133, Rome, Italy
[6] INAF Osservatorio Astronomico di Roma, Via di Frascati 33, I-00040, Monteporzio Catone, Rome, Italy
[7] Department of Mathematics, Informatics, Physical and Geophysical Sciences, University of Messina, Via F.S. D'Alcontres 31, Messina, I-98166, Italy
[8] Space Research Institute of RAS, Profsoyuznaya, 84/32, Moscow 117997, Russia
[9] National Research University Higher School of Economics, Myasnitskaya 20, Moscow 101000, Russia
[10] Moscow Institute of Physics and Technology (MIPT), Institutskiy Pereulok, 9, Dolgoprudny 141701, Russia
[11] CAS Key Laboratory of Space Astronomy and Technology, National Astronomical Observatories, Chinese Academy of Sciences, Beijing 100101, People's Republic of China
[12] INAF-IAPS, via Fosso del Cavaliere 100, I-00133, Rome, Italy
[13] INAF-OAS, via Gobetti 93/3, I-40129, Bologna, Italy
[14] INFN Roma La Sapienza, Piazzale A. Moro 2, I-00185, Rome, Italy
[15] Department of Physics and Astronomy, Michigan State University, East Lansing, MI 48824, USA
[16] University of Michigan, Randall Laboratory of Physics, 450 Church Street, Ann Arbor, MI 48109-1040, USA
[17] School of Astronomy and Space Science, Nanjing University, Nanjing, People's Republic of China
[18] Taurus Hill Observatory, Härkämäentie 88, FI-79480 Kangaslampi, Finland
[19] Institute of Solar-Terrestrial Physics, Russian Academy of Sciences, Siberian Branch, Irkutsk, Russia
[20] Mullard Space Science Laboratory, University College London, Holmbury St Mary, Surrey, UK
[21] Steward Observatory, The University of Arizona, Tucson, AZ 85721, USA
[22] Crimean Astrophysical Observatory, Russian Academy of Sciences, Nauchnyi 298409, Russia
[23] SLAC National Accelerator Laboratory, Menlo Park, CA 94025, USA
[24] Department of Physics & Astronomy, Louisiana State University, Baton Rouge, LA 70803, USA
[25] Space Research Institute of the Russian Academy of Sciences (IKI), 84/32 Profsoyuznaya Str., Moscow 117997, Russia
[26] Purple Mountain Observatory, Chinese Academy of Sciences, Nanjing, People's Republic of China
[27] Nevada Center for Astrophysics, University of Nevada, Las Vegas, NV 89154, USA
[28] Department of Physics and Astronomy, University of Nevada, Las Vegas, NV 89154, USA
Received 2022 April 24; revised 2022 August 28; accepted 2022 September 16; published 2022 November 1

Abstract

We obtained well-sampled optical photometry of GRB 110213A, including Swift/UVOT and XRT. Combining our data from those of other ground-based telescopes, we present 15 optical multicolor light curves showing similar shapes with two peaks. In contrast, in the X-ray band, only a single peak is observed between the two optical peaks. Temporal and spectral analysis of GRB 110213A shows that the X-rays differ from the optical for Phases I–III (before the second peak of the optical band at ∼5.6 ks). Moreover, they have the same spectral behavior at late times (Phases IV–VI). These data indicate that the optical and X-ray emission are dominated by different components. The synchrotron-supported pair cascade emission is included in the standard external forward-shock model, which is dominated by synchrotron radiation and synchrotron self-Compton (SSC). We find that the optical bands of GRB 110213A are dominated by the cascade emission from synchrotron radiation + SSC at the early stage, while the primary synchrotron + SSC radiation dominates the X-ray band. At late stages, both the X-ray and optical bands are dominated by emission from primary synchrotron + SSC radiation. The cascade component can reasonably explain the first optical peak. In contrast, the primary synchrotron + SSC emission mainly contributes to the second peak.

Unified Astronomy Thesaurus concepts: Gamma-ray bursts (629)

1. Introduction

At electromagnetic wavelengths, gamma-ray bursts (GRBs) are the most luminous stellar phenomena in the universe. Owing to observational detectors launched successfully, our understanding of the origins of GRBs is becoming progressively more profound (e.g., Gehrels et al. 2004; Zhang & Mészáros 2004; Burrows et al. 2005; Roming et al. 2005; Atwood et al. 2009; Meegan et al. 2009; Kumar & Zhang 2015; Wang et al. 2015; Dai et al. 2017; Warren et al. 2017; Zhang et al. 2018, 2020; Li et al. 2020). One of the most popular models of GRBs is the standard fireball model (Mészáros 2002; Piran 2004; Zhang & Mészáros 2004), which proposes that the

prompt gamma-ray emission can be explained by internal dissipative processes (Meszaros & Rees 1993; Rees & Meszaros 1994) and the multiband afterglow is produced by synchrotron emission from the external shock when the fireball is decelerated by the ambient medium (Mészáros & Rees 1997; Sari et al. 1998; Wang et al. 2018; Du et al. 2021).

Recent multiwavelength observations of GRBs have revealed diverse features of their X-ray and optical afterglow light curves (e.g., Panaitescu et al. 2006; Zhang et al. 2006; Panaitescu & Vestrand 2011; Li et al. 2012; Liang et al. 2013). They found that a mixture of different components accounts for their diverse light curves. The X-ray light curves appear to have five temporal components (Zhang et al. 2006): steep decay Phase I, which is associated with the prompt emission (Barthelmy et al. 2005; Tagliaferri et al. 2005; Zhang et al. 2007); shallow-decay Phase II, which involves the energy injection (Nousek et al. 2006; Zhang et al. 2006; Liang et al. 2007; De Pasquale et al. 2016); normal decay Phase III, which is predicted by the external forward-shock model; post-jet-break Phase IV, which has a jet-break origin (e.g., Liang et al. 2008; Racusin et al. 2009); and flares V (Burrows et al. 2005; Fan & Wei 2005; Ioka et al. 2005; Liang et al. 2006; Zhang et al. 2006; Chincarini et al. 2007; Lazzati & Perna 2007; Maxham & Zhang 2009; Margutti et al. 2010). Components II, III, and IV can be interpreted with the external-shock models, while components I and V need to invoke the internal models. Li et al. (2012) and Liang et al. (2013) proposed that there are eight possible emission components in the *synthetic* light curve: Ia, prompt optical flares; Ib, an early optical flare from the reverse shock; II, early shallow-decay segment; III, standard afterglow component (an onset hump followed by a normal decay segment); IV, post-jet-break phase; V, optical flares; VI, rebrightening humps; and VII, late supernova (SN) bumps. Components II–V can find their counterparts in the canonical X-ray light curve. Most of the multiwavelength afterglow can be interpreted in the frame of external-shock models (e.g., Kann et al. 2006, 2010, 2011; Nardini et al. 2006; Panaitescu & Vestrand 2008, 2011; Maselli et al. 2014; Perley et al. 2014; Wang et al. 2015; Huang et al. 2018; Li et al. 2020). However, many GRBs require advanced modeling, e.g., long-lasting reverse shock, structured jets, arbitrary circumburst medium density profile (e.g., Fan & Piran 2006; Panaitescu et al. 2006; Huang et al. 2007; Liang et al. 2007, 2008; Kumar et al. 2008; Nardini et al. 2011; Greiner et al. 2013; Hou et al. 2014; Melandri et al. 2014; De Pasquale et al. 2015; Laskar et al. 2015; Wang et al. 2015; Xie et al. 2020).

The high-energy photons may be absorbed via the $\gamma\gamma \rightarrow e^{+}e^{-}$ pair-production process in the synchrotron radiation and synchrotron self-Compton (SSC) of the GRB fireball model. Furthermore, the secondary $e^{+}e^{-}$ pairs could produce cascade emission via the synchrotron radiation and SSC processes (e.g., Moderski et al. 2005; Böttcher et al. 2013; Veres et al. 2017). The synchrotron-supported cascade has been used to interpret the physical origins of high-energy astrophysical objects such as GRBs and blazars (e.g., Pe'er & Waxman 2005; Aharonian et al. 2008; Zacharopoulou et al. 2011; Böttcher et al. 2013; Yan & Zhang 2015; Gill & Granot 2018; Huang et al. 2021). Huang et al. (2021) presented a comparative analysis of the SSC emission of GRB afterglows in homogeneous and wind environments within the framework of the forward-shock model. The $\gamma\gamma$ absorption of very-high-energy photons owing to pair production within the source and the Klein–Nishina effect on inverse-Compton (IC) scattering are considered in their work. They found that the cascade emission resulting from the absorbed high-energy photons could be comparable to the synchrotron emission of primary electrons in the optical band, which may explain the optical and X-ray afterglow light curves at early times.

GRB 110213A is an interesting GRB, with 15 optical multiband light curves showing similar shapes having two peaks. However, only one peak is seen in the X-ray band, and it occurs between the two peaks in the optical, suggesting that the optical and X-ray emission are dominated by different components. Synchrotron-supported pair cascade emission is included in the standard external forward-shock model to explain the chromatic behavior of the GRB 110213A afterglow.

This paper is organized as follows. Our observations and data reduction are reported in Section 2. Section 3 presents an analysis of the optical and X-ray data. The modeling method and results are presented in Section 4. We provide a discussion and our conclusions in Section 5. Throughout, we adopt a standard cosmological model with $H_0 = 71$ km s^{-1} Mpc^{-1}, $\Omega_M = 0.27$, and $\Omega_\Lambda = 0.73$. We use the usual power-law representation of flux density, $F(\nu) \propto t^{-\alpha}\nu^{-\beta}$, where α is the temporal-decay index and β is the spectral index. All uncertainties are given at 1σ confidence level unless otherwise stated.

2. Observations and Data Reduction

2.1. Observations

At 05:17:29 on 2011 February 13 (T_0; UT dates are used throughout this paper), the Swift/BAT triggered and located GRB 110213A (trigger = 445414). We obtained Swift/UVOT data from $T_0 + 75.6$–342,659 s after the trigger, and Swift/XRT data from $T_0 + 82$–485,650 s. The BAT light curve shows a single-peaked structure with T_{90} (15–350 keV) = 48 ± 16 s (estimated uncertainty including systematics). The outburst was also detected by Konus-Wind (Golenetskii et al. 2011) in the gamma-ray band. A bright, uncatalogued X-ray afterglow was promptly identified by Swift/XRT (Burrows et al. 2005) 91.7 s after the burst. The Swift/UVOT (Roming et al. 2005) revealed an optical afterglow 100 s after the burst at J2000 location (α, δ) = ($02^{\rm h}51^{\rm m}51\overset{\rm s}{.}40$, $+49°16'23\overset{''}{.}6$) with a 90% confidence error radius of $0\overset{''}{.}61$.

ROTSE-IIIb, located at the McDonald Observatory in Texas, responded to GRB 110213A promptly and confirmed the optical afterglow (Rujopakarn et al. 2011). The first image started at 05:17:57, 28 s after the burst (0.7 s after the GCN notification time). The optical afterglow was observed to rebrighten dramatically to ~17.0 mag about 200 s after the burst. ROTSE-IIIb continued to monitor the afterglow until it was no longer detectable, ~1.9 hr after the trigger.

Ground-based optical follow-up observations have also been performed by different groups with various instruments such as Lick/KAIT, the Palomar 60 inch telescope, and the Gemini-North telescope (Cucchiara et al. 2011). We use those data here along with our own photometry from the following facilities: 0.51 m Global Rent-a-Scope (GRAS) 011 telescope in Mayhill, New Mexico (Hentunen et al. 2011a); 0.61 m Lightbuckets rental telescope LB-0001 in Rodeo, New Mexico (Ukwatta et al. 2011); 1.6 m AZT-33IK telescope at Sayan Solar Observatory, Mondy (Volnova et al. 2011); 1.25 m AZT-11

telescope at CrAO (Rumyantsev et al. 2011); 0.356 m Celestron C14 XLT telescope at Taurus Hill Observatory, Finland (Hentunen et al. 2011b); and 0.8 m TNT (Xin et al. 2011) at Xinglong Observatory, China (Zheng et al. 2008; Xin et al. 2010).

The redshift measurement of GRB 110213A ($z = 1.4607$) was reported by Milne & Cenko (2011), obtained with the 2.3 m Bok telescope; see also Cucchiara et al. (2011). We adopt this redshift value in our calculations.

2.2. Data Reduction

The Swift data were processed with the standard HEAsoft software (version 6.10). The XRT data were further automatically processed by the GRB light-curve repository pipeline[29] (Evans et al. 2007, 2009, 2010), with the background subtracted. For the XRT, the windowed timing and photon counting data were processed separately. Pile-up corrections were applied if necessary, especially at early times when the source was very bright.

Swift UVOT observations started 82 s after the trigger, with 9.6 s exposures in v; there appear to be no significant problems of trailing or cathode voltage ramp-up. The extended point-spread function of a blue, nearby, $V = 16$ mag source, which was an issue once the GRB became faint, was taken into account by reducing the aperture of the extraction to $3''$ and by positioning the background extraction at the same distance as the GRB (but at a different position angle). The UVOT data were summed to a minimum signal-to-noise ratio (S/N) of 2, keeping the $\log(t/\mathrm{s})$ bin size limited to 0.3. The UVOT magnitudes and fluxes are given in Table 1, where the flux is determined from the magnitudes using a UVOT GRB spectral model (Poole et al. 2008; Breeveld et al. 2010, 2011).

For the ground-based optical data, different methods were used for each instrument. For the ROTSE data, the raw images were processed using the standard ROTSE software pipeline. Image coaddition was performed if necessary to obtain a reasonable S/N (e.g., minimum of 3). Photometry was then extracted using the method described by Quimby et al. (2006). Other optical data were processed using standard procedures provided by IRAF[30] software. Differential aperture photometry was performed with the DAOPHOT package in IRAF. Reference stars in the R band were calibrated using data from the USNO B2.0 catalog. *Clear*(C)-band data were calibrated to the R band, which generally provides the best match (Li et al. 2003). Our ground-based photometry is listed in Table 2. In addition, in our analysis, we use all of the GRB 110213A data published by Cucchiara et al. (2011), except their UVOT results.

3. Data Analysis

Generally, the GRB afterglow temporal behavior can be fit with a single power-law function or broken-power-law functions or multiple broken-power-law function, which have been widely adopted for fitting afterglow light curves during both the rising and decay phases and work well in most cases (e.g., Rykoff et al. 2009; Liang et al. 2010; Wang et al. 2015, 2018). Here, we fit the complicated light curves of GRB 110213A with broken-power-law and multiple broken-power-law models for X-ray and optical light curves, respectively. The broken power-law function can be represented as

$$f = A\left(\frac{t}{t_b}\right)^{\alpha_1}\left[1+\left(\frac{t}{t_b}\right)^{s(\alpha_1-\alpha_2)}\right]^{-1/s}, \quad (1)$$

where f is the flux, A is the scale constant, t_b is the break time, α_1 and α_2 are the two power-law indices before and after the break, and s is a smoothing parameter. According to this definition, the peak time t_p, where the flux reaches its maximum, is

$$t_p = t_b\left(\frac{\alpha_1}{-\alpha_2}\right)^{1/[s(\alpha_1-\alpha_2)]}. \quad (2)$$

If more breakpoints are required to represent the light curve, Equation (1) can be modified to be

$$f = A\left(\frac{t}{t_{b1}}\right)^{\alpha_1}\left[1+\left(\frac{t}{t_{b1}}\right)^{s_1(\alpha_1-\alpha_2)}\right]^{-1/s_1} \times\left[1+\left(\frac{t}{t_{b2}}\right)^{s_2(\alpha_2-\alpha_3)}\right]^{-1/s_2}. \quad (3)$$

The fitting results of GRB 110213A afterglow are shown in Figure 1. The most obvious characteristic of the optical multiband light curves is that they exhibit an unusual two-peak profile. The first bump has a rising index $\alpha_{O,1}\approx -2.46$, peaks at $\sim$213 s, and then decays with index $\alpha_{O,2}\approx 0.98$. The second bump has a rising index $\alpha_{O,3}\approx -1.12$, peaks at $\sim$5.6 ks, and decays sharply thereafter with index $\alpha_{O,4}\approx 1.61$. The X-ray light curve, in contrast, has only a single peak with a rising index of ~ -0.93, peaking at $\sim$1.4 ks, and then decaying with an index $\sim$1.63. The optical and X-ray light curves exhibit obvious chromatic effects before $\sim$5.6 ks, but thereafter they have similar temporal behavior. These results indicate that the optical and X-ray emission are dominated by different components.

To get more information, an analysis of the broadband spectral energy distribution (SED) must be conducted. The optical data were corrected for Galactic extinction based on the burst direction (Schlegel et al. 1998), with $A_V = 0.127$ mag, $A_R = 0.102$ mag, $A_I = 0.074$ mag, $A_g = 0.145$ mag, and $A_i = 0.080$ mag. We use the Xspec package to fit the spectrum with an absorbed single power law by fixing the equivalent hydrogen column density of our Milky Way in the burst direction as $N_{\rm H}^{\rm MW} = 3.44\times10^{21}$ cm^{-2}. The extinction law of the host galaxy was taken to be that of the Small Magellanic Cloud ($R_V = 2.93$). We obtain an $N_{\rm H}$ value in the host galaxy as $N_{\rm H}^{\rm host} = 3\times10^{20}$ cm^{-2}, and fixed at this value in our time-resolved spectral fits. Noting that since the redshift for the GRB is $z = 1.46$, Lyα affects the data in the ultraviolet (UV) bands of UVOT (*uvw2*, *uvm2*, and *uvw1*); thus, these three bands are not included in the spectral fitting. The $E(B-V)$ value from the Galactic extinction is set to 0.43 mag (Schlegel et al. 1998) during the fitting.

Spectral fitting was performed using the "Xspec" package with a single power-law function for the optical and X-ray afterglows. We subdivided the broadband data into six time intervals (as marked in Figure 1): T_0 + [0.15, 0.3], [0.3, 0.7], [0.7, 2.0], [2.0, 5.6], [5.6, 30], and [30, 500] ks, which are respectively recorded as Phases I–VI. Phases I and II cover the

[29] http://www.swift.ac.uk/xrt_curves/

[30] IRAF is distributed by NOAO, which is operated by AURA, Inc., under a cooperative agreement with the National Science Foundation (NSF).

Table 1
Swift/UVOT Photometric Observations of GRB 110213A

$T - T_0$ (s)[a]	Exp. (s)	Mag	1σ[b]	Flux (μJy)	1σ[c]	Filter	$T - T_0$ (s)	Exp. (s)	Mag	1σ[b]	Flux (μJy)	1σ[c]	Filter
84.42	2.50	16.79	0.55	7.01e-01	3.42e-01	*v*	1925.11	9.87	16.21	0.135	1.20e+00	1.48e-01	*v*
89.28	2.36	16.56	0.50	8.63e-01	3.87e-01	*v*	2098.02	9.88	16.48	0.159	9.31e-01	1.36e-01	*v*
644.65	2.27	15.31	0.18	2.73e+00	4.55e-01	*v*	2272.23	9.88	16.70	0.179	7.62e-01	1.25e-01	*v*
649.42	2.50	15.50	0.19	2.30e+00	3.87e-01	*v*	2445.37	9.88	16.46	0.158	9.46e-01	1.37e-01	*v*
654.42	2.50	16.00	0.25	1.45e+00	3.29e-01	*v*	2618.84	9.88	16.43	0.153	9.77e-01	1.37e-01	*v*
659.42	2.50	16.09	0.26	1.33e+00	3.24e-01	*v*	6782.34	99.89	16.30	0.050	1.10e+00	5.10e-02	*v*
816.28	0.64	16.58	0.66	8.52e-01	5.13e-01	*v*	8218.34	99.89	16.51	0.055	9.06e-01	4.59e-02	*v*
819.42	2.50	16.05	0.25	1.38e+00	3.24e-01	*v*	24339.37	149.89	18.21	0.132	1.89e-01	2.30e-02	*v*
824.42	2.50	15.78	0.22	1.77e+00	3.54e-01	*v*	24644.61	149.89	18.42	0.155	1.55e-01	2.21e-02	*v*
829.42	2.50	16.44	0.32	9.65e-01	2.83e-01	*v*	24948.05	149.89	18.23	0.134	1.86e-01	2.29e-02	*v*
833.66	1.74	16.15	0.32	1.25e+00	3.61e-01	*v*	42365.24	453.44	19.450	0.158	6.05e-02	8.77e-03	*v*
1049.49	2.43	15.84	0.23	1.67e+00	3.26e-01	*v*	53517.77	453.51	20.020	0.248	3.58e-02	8.17e-03	*v*
1054.42	2.50	16.27	0.28	1.13e+00	2.99e-01	*v*	111151.25	6093.88	21.06	0.488	1.36e-02	6.14e-03	*v*
1059.42	2.50	16.22	0.27	1.18e+00	2.98e-01	*v*	226673.37	69391.31	21.95	0.687	6.06e-03	3.83e-03	*v*
1064.38	2.46	15.92	0.23	1.55e+00	3.29e-01	*v*	42365.24	453.44	19.45	0.158	6.05e-02	8.77e-03	*v*
1231.02	9.88	15.98	0.12	1.47e+00	1.60e-01	*v*	53517.77	453.51	20.02	0.248	3.58e-02	8.17e-03	*v*
1404.21	9.88	16.00	0.12	1.45e+00	1.62e-01	*v*	111151.25	6093.88	21.06	0.488	1.36e-02	6.14e-03	*v*
1577.01	9.88	16.34	0.15	1.05e+00	1.43e-01	*v*	226673.37	69391.31	21.95	0.687	6.06e-03	3.83e-03	*v*
1751.36	9.88	16.32	0.14	1.07e+00	1.43e-01	*v*	…	…	…	…	…	…	…
577.91	9.89	16.12	0.08	1.44e+00	9.41e-02	*b*	2544.02	9.88	17.10	0.121	5.87e-01	5.87e-02	*b*
751.10	9.88	16.51	0.09	1.00e+00	7.82e-02	*b*	6167.10	99.87	16.87	0.044	7.27e-01	2.63e-02	*b*
1155.35	9.89	16.72	0.10	8.28e-01	6.80e-02	*b*	7603.08	99.86	17.16	0.044	5.55e-01	2.01e-02	*b*
1330.02	9.88	16.92	0.11	6.90e-01	6.30e-02	*b*	13611.98	149.89	17.83	0.053	2.98e-01	1.29e-02	*b*
1502.83	9.88	16.97	0.11	6.63e-01	6.22e-02	*b*	13915.54	149.89	17.82	0.052	3.03e-01	1.30e-02	*b*
1675.97	9.88	16.95	0.11	6.72e-01	6.20e-02	*b*	14155.17	86.08	17.94	0.071	2.71e-01	1.60e-02	*b*
1850.84	9.88	17.10	0.12	5.86e-01	5.93e-02	*b*	31241.06	338.29	19.61	0.102	5.78e-02	4.86e-03	*b*
2023.49	9.88	17.29	0.14	4.90e-01	5.53e-02	*b*	131612.00	37125.87	21.87	0.521	7.24e-03	3.12e-03	*b*
2196.65	9.88	17.11	0.12	5.79e-01	5.87e-02	*b*	275250.71	89466.84	22.37	0.479	4.55e-03	1.80e-03	*b*
2371.10	9.85	16.93	0.11	6.85e-01	6.31e-02	*b*	…	…	…	…	…	…	…
314.93	2.50	15.51	0.16	9.04e-01	1.22e-01	*u*	509.93	2.50	15.27	0.138	1.12e+00	1.33e-01	*u*
319.93	2.50	15.33	0.15	1.06e+00	1.30e-01	*u*	514.93	2.50	15.56	0.157	8.59e-01	1.15e-01	*u*
324.93	2.50	15.30	0.14	1.09e+00	1.33e-01	*u*	519.93	2.50	15.82	0.180	6.77e-01	1.03e-01	*u*
329.93	2.50	15.50	0.16	9.10e-01	1.22e-01	*u*	524.93	2.50	15.57	0.158	8.52e-01	1.15e-01	*u*
334.93	2.50	15.63	0.17	8.11e-01	1.15e-01	*u*	529.93	2.50	15.81	0.176	6.84e-01	1.03e-01	*u*
339.93	2.50	15.53	0.16	8.84e-01	1.21e-01	*u*	534.93	2.50	15.91	0.187	6.23e-01	9.83e-02	*u*
344.93	2.50	15.41	0.15	9.93e-01	1.24e-01	*u*	539.93	2.50	15.73	0.168	7.37e-01	1.04e-01	*u*
349.93	2.50	15.47	0.15	9.34e-01	1.22e-01	*u*	544.93	2.50	15.67	0.167	7.77e-01	1.10e-01	*u*
354.93	2.50	15.66	0.17	7.86e-01	1.15e-01	*u*	549.93	2.50	15.49	0.152	9.20e-01	1.17e-01	*u*
359.93	2.50	15.45	0.15	9.50e-01	1.23e-01	*u*	554.93	2.50	15.94	0.188	6.07e-01	9.75e-02	*u*
364.93	2.50	15.82	0.19	6.81e-01	1.05e-01	*u*	559.81	2.38	15.77	0.177	7.13e-01	1.05e-01	*u*
369.93	2.50	15.94	0.20	6.10e-01	1.02e-01	*u*	716.89	0.54	16.34	0.482	4.22e-01	1.72e-01	*u*
374.93	2.50	15.57	0.16	8.58e-01	1.20e-01	*u*	719.93	2.50	15.99	0.191	5.81e-01	9.31e-02	*u*
379.93	2.50	15.87	0.19	6.47e-01	1.03e-01	*u*	724.93	2.50	15.74	0.166	7.33e-01	1.03e-01	*u*
384.93	2.50	15.70	0.17	7.57e-01	1.09e-01	*u*	729.93	2.50	16.28	0.217	4.43e-01	8.07e-02	*u*
389.93	2.50	15.53	0.16	8.88e-01	1.17e-01	*u*	734.28	1.84	16.11	0.235	5.22e-01	1.04e-01	*u*
394.93	2.50	15.58	0.16	8.43e-01	1.16e-01	*u*	1130.55	9.88	16.55	0.124	3.47e-01	3.64e-02	*u*
399.93	2.50	15.50	0.16	9.10e-01	1.22e-01	*u*	1305.15	9.88	16.43	0.116	3.88e-01	3.82e-02	*u*
404.93	2.50	15.46	0.15	9.46e-01	1.23e-01	*u*	1478.02	9.88	16.92	0.152	2.46e-01	3.17e-02	*u*
409.93	2.50	15.41	0.15	9.94e-01	1.23e-01	*u*	1651.11	9.88	16.58	0.125	3.37e-01	3.57e-02	*u*
414.93	2.50	15.42	0.15	9.83e-01	1.23e-01	*u*	1825.90	9.89	16.45	0.116	3.81e-01	3.77e-02	*u*
419.93	2.50	15.57	0.16	8.51e-01	1.17e-01	*u*	1998.73	9.88	16.64	0.130	3.18e-01	3.51e-02	*u*
424.93	2.50	15.77	0.18	7.08e-01	1.05e-01	*u*	2171.61	9.88	16.73	0.136	2.92e-01	3.37e-02	*u*
429.93	2.50	15.66	0.17	7.89e-01	1.11e-01	*u*	2346.16	9.88	16.63	0.130	3.20e-01	3.52e-02	*u*
434.93	2.50	15.61	0.17	8.22e-01	1.15e-01	*u*	2519.13	9.88	16.49	0.119	3.65e-01	3.69e-02	*u*
439.93	2.50	15.63	0.17	8.09e-01	1.11e-01	*u*	5960.94	99.89	16.53	0.052	3.53e-01	1.54e-02	*u*
444.93	2.50	15.78	0.18	7.04e-01	1.05e-01	*u*	7397.90	99.88	16.80	0.050	2.75e-01	1.15e-02	*u*
449.93	2.50	15.57	0.16	8.58e-01	1.16e-01	*u*	12699.17	149.89	17.36	0.055	1.65e-01	7.70e-03	*u*
454.93	2.50	15.75	0.17	7.24e-01	1.05e-01	*u*	13002.76	149.88	17.41	0.056	1.57e-01	7.47e-03	*u*
459.93	2.50	15.66	0.17	7.89e-01	1.11e-01	*u*	13306.38	149.88	17.52	0.059	1.41e-01	7.12e-03	*u*
464.93	2.50	15.60	0.16	8.34e-01	1.11e-01	*u*	19468.20	149.89	18.36	0.096	6.52e-02	5.33e-03	*u*
469.93	2.50	15.68	0.17	7.69e-01	1.10e-01	*u*	19771.70	149.89	18.20	0.086	7.55e-02	5.52e-03	*u*
474.93	2.50	15.77	0.18	7.09e-01	1.05e-01	*u*	19973.40	47.93	18.26	0.155	7.19e-02	9.44e-03	*u*
479.93	2.50	15.56	0.16	8.65e-01	1.16e-01	*u*	30443.57	453.45	19.08	0.088	3.37e-02	2.50e-03	*u*
484.93	2.50	15.74	0.17	7.28e-01	1.05e-01	*u*	37130.66	228.12	19.26	0.130	2.86e-02	3.15e-03	*u*

Table 1
(Continued)

$T-T_0$ (s)[a]	Exp. (s)	Mag	1σ[b]	Flux (μJy)	1σ[c]	Filter	$T-T_0$ (s)	Exp. (s)	Mag	1σ[b]	Flux (μJy)	1σ[c]	Filter
489.93	2.50	15.46	0.15	9.42e-01	1.21e-01	*u*	48553.35	363.01	19.65	0.136	1.99e-02	2.30e-03	*u*
494.93	2.50	15.70	0.17	7.56e-01	1.08e-01	*u*	102238.79	8665.93	21.45	0.373	3.79e-03	1.20e-03	*u*
499.93	2.50	15.61	0.16	8.26e-01	1.11e-01	*u*	226073.88	69328.20	22.65	0.907	1.25e-03	9.67e-04	*u*
504.93	2.50	15.91	0.19	6.26e-01	9.89e-02	*u*	…	…	…	…	…	…	…
102.83	2.50	17.69	0.31	1.63e-01	3.38e-02	*white*	242.83	2.50	16.10	0.107	7.07e-01	5.03e-02	*white*
107.83	2.50	17.76	0.32	1.52e-01	3.26e-02	*white*	247.72	2.38	15.92	0.101	8.31e-01	5.64e-02	*white*
112.83	2.50	17.64	0.30	1.71e-01	3.45e-02	*white*	593.84	1.50	16.16	0.126	6.69e-01	5.66e-02	*white*
117.83	2.50	17.33	0.23	2.27e-01	3.48e-02	*white*	597.83	2.50	16.20	0.100	6.41e-01	4.31e-02	*white*
122.83	2.50	17.57	0.28	1.82e-01	3.44e-02	*white*	602.83	2.50	16.21	0.100	6.35e-01	4.24e-02	*white*
127.83	2.50	17.16	0.21	2.65e-01	3.78e-02	*white*	607.83	2.50	16.24	0.101	6.19e-01	4.21e-02	*white*
132.83	2.50	17.02	0.19	3.01e-01	3.88e-02	*white*	611.22	0.88	16.31	0.175	5.83e-01	6.84e-02	*white*
137.83	2.50	16.92	0.18	3.30e-01	3.90e-02	*white*	768.02	2.32	16.37	0.109	5.51e-01	4.01e-02	*white*
142.83	2.50	16.56	0.14	4.63e-01	4.35e-02	*white*	772.83	2.50	16.50	0.111	4.89e-01	3.67e-02	*white*
147.83	2.50	16.62	0.15	4.38e-01	4.30e-02	*white*	777.83	2.50	16.52	0.112	4.77e-01	3.58e-02	*white*
152.83	2.50	16.60	0.15	4.44e-01	4.36e-02	*white*	782.83	2.50	16.23	0.099	6.27e-01	4.14e-02	*white*
157.83	2.50	16.55	0.14	4.67e-01	4.36e-02	*white*	1170.08	0.26	16.89	0.404	3.41e-01	9.24e-02	*white*
162.83	2.50	16.52	0.14	4.80e-01	4.53e-02	*white*	1172.83	2.50	16.77	0.122	3.78e-01	3.07e-02	*white*
167.83	2.50	16.35	0.13	5.58e-01	4.68e-02	*white*	1177.83	2.50	16.64	0.113	4.29e-01	3.26e-02	*white*
172.83	2.50	16.37	0.13	5.52e-01	4.67e-02	*white*	1182.83	2.50	16.63	0.114	4.32e-01	3.29e-02	*white*
177.83	2.50	16.35	0.13	5.61e-01	4.78e-02	*white*	1187.45	2.12	16.64	0.123	4.30e-01	3.51e-02	*white*
182.83	2.50	16.31	0.12	5.83e-01	4.76e-02	*white*	1354.44	9.87	16.77	0.064	3.79e-01	1.62e-02	*white*
187.83	2.50	16.30	0.12	5.86e-01	4.77e-02	*white*	1527.24	9.88	16.88	0.067	3.43e-01	1.54e-02	*white*
192.83	2.50	16.07	0.11	7.27e-01	5.22e-02	*white*	1700.34	9.88	16.87	0.066	3.46e-01	1.53e-02	*white*
197.83	2.50	16.19	0.11	6.50e-01	4.99e-02	*white*	1875.25	9.88	17.05	0.072	2.93e-01	1.42e-02	*white*
202.83	2.50	16.27	0.12	6.03e-01	4.86e-02	*white*	2048.16	9.88	16.94	0.068	3.26e-01	1.49e-02	*white*
207.83	2.50	16.18	0.11	6.53e-01	4.98e-02	*white*	2221.24	9.88	16.90	0.067	3.36e-01	1.51e-02	*white*
212.83	2.50	16.13	0.11	6.84e-01	5.11e-02	*white*	2395.50	9.88	16.95	0.069	3.23e-01	1.48e-02	*white*
217.83	2.50	16.16	0.11	6.64e-01	5.08e-02	*white*	2568.95	9.88	16.94	0.068	3.24e-01	1.48e-02	*white*
222.83	2.50	16.04	0.11	7.45e-01	5.18e-02	*white*	6371.81	99.89	16.88	0.029	3.44e-01	6.81e-03	*white*
227.83	2.50	16.19	0.11	6.50e-01	4.91e-02	*white*	7807.90	99.89	17.06	0.029	2.92e-01	5.74e-03	*white*
232.69	2.35	16.09	0.11	7.09e-01	5.30e-02	*white*	183368.82	26266.40	22.47	0.455	1.99e-03	6.10e-04	*white*
238.02	2.31	16.04	0.11	7.42e-01	5.42e-02	*white*	342658.85	98663.58	23.78	0.736	5.99e-04	2.96e-04	*white*
701.88	9.89	16.46	0.18	2.28e-01	3.97e-02	*uvw1*	12091.65	449.88	18.29	0.081	4.24e-02	3.40e-03	*uvw1*
1193.53	97.18	17.24	0.18	1.11e-01	1.99e-02	*uvw1*	18861.90	449.89	19.56	0.141	1.31e-02	1.84e-03	*uvw1*
1540.12	96.49	17.59	0.22	8.07e-02	1.75e-02	*uvw1*	29533.79	449.87	20.22	0.231	7.15e-03	1.63e-03	*uvw1*
1887.55	96.77	17.24	0.18	1.11e-01	2.00e-02	*uvw1*	36446.23	449.89	20.00	0.183	8.72e-03	1.58e-03	*uvw1*
2320.90	183.67	17.50	0.19	8.73e-02	1.64e-02	*uvw1*	47733.75	449.89	21.33	0.525	2.56e-03	1.33e-03	*uvw1*
2668.12	9.88	17.32	0.26	1.03e-01	2.67e-02	*uvw1*	136705.75	44039.05	22.64	0.817	7.73e-04	6.26e-04	*uvw1*
7192.24	99.89	17.78	0.11	6.78e-02	7.64e-03	*uvw1*	…	…	…	…	…	…	…
676.82	9.88	18.25	0.54	3.87e-02	1.70e-02	*uvm2*	6987.14	99.89	18.40	0.184	3.40e-02	5.09e-03	*uvm2*
850.01	9.88	17.88	0.43	5.45e-02	1.90e-02	*uvm2*	8392.73	69.23	18.67	0.255	2.65e-02	5.50e-03	*uvm2*
1081.38	9.88	18.22	0.53	4.00e-02	1.73e-02	*uvm2*	17954.54	449.88	20.78	0.357	3.78e-03	1.09e-03	*uvm2*
1689.10	270.34	19.02	0.40	1.91e-02	6.07e-03	*uvm2*	36189.96	11086.95	22.19	0.635	1.02e-03	5.31e-04	*uvm2*
2296.13	183.73	18.91	0.45	2.11e-02	7.70e-03	*uvm2*	…	…	…	…	…	…	…
627.69	9.89	17.96	0.37	4.99e-02	1.65e-02	*uvw2*	2421.12	183.10	19.26	0.442	1.50e-02	5.92e-03	*uvw2*
801.03	9.88	18.40	0.46	3.32e-02	1.35e-02	*uvw2*	6577.60	99.89	18.76	0.184	2.39e-02	3.92e-03	*uvw2*
1119.65	96.97	19.10	0.47	1.74e-02	7.22e-03	*uvw2*	8013.69	99.89	19.27	0.240	1.49e-02	3.20e-03	*uvw2*
1726.58	356.72	19.78	0.47	9.34e-03	3.90e-03	*uvw2*	52607.15	449.88	21.65	0.644	1.67e-03	9.62e-04	*uvw2*

Notes.
[a] $T-T_0$ is the midpoint of each observation. The reference time T_0 is the Swift/BAT burst trigger time.
[b] 1σ is the uncertainty in the magnitude.
[c] 1σ is the uncertainty in the flux.

rise and decay of the first peak of the optical multiband light curves, respectively. Phase III spans the peak of the X-ray afterglow, while Phases IV and V, respectively, cover the rise and decay of the second peak. Finally, Phase VI represents the late-time afterglow, where the X-ray and optical multiband light curves have the same temporal behavior.

The X-ray spectrum can be well fit with a power-law model; the results are presented in Figure 2 and Table 3. The corresponding derived photon indices are 2.08, 1.91, 1.94, 1.79, 2.07, and 2.09 for (respectively) Phases I–VI. One can see that the spectral indices of the X-ray band are roughly the same, with no obvious spectral evolution. We extrapolate the fitting line from the X-rays to the optical bands, also as shown in Figure 2. Clearly, the X-ray spectrum differs from the optical for Phases I–III (before the second peak in the optical bands, ∼5.6 ks). They have the same (achromatic) spectral behaviors

Table 2
Ground-based Telescope Photometry of GRB 110213A

$T - T_0$ (s)[a]	Exp. (s)	Mag	1σ[b]	Filter	$T - T_0$ (s)	Exp (s)	1σ[b]	Error	Filter
				ROTSE-IIIb					
75.60	2.59	16.78	0.15	*C*	3068.32	10.37	16.03	0.07	*C*
86.83	2.59	17.12	0.21	*C*	3097.18	10.37	16.44	0.11	*C*
98.24	2.59	16.46	0.09	*C*	3154.90	10.37	16.32	0.11	*C*
109.64	2.59	16.26	0.13	*C*	3183.75	10.37	15.95	0.11	*C*
121.05	2.59	16.19	0.12	*C*	3198.79	140.83	16.09	0.04	*C*
153.79	10.37	15.41	0.04	*C*	3213.04	10.37	16.16	0.11	*C*
182.74	10.37	15.37	0.05	*C*	3241.90	10.37	16.03	0.10	*C*
211.68	10.37	15.02	0.02	*C*	3270.76	10.37	16.18	0.08	*C*
240.97	10.37	14.96	0.02	*C*	3329.25	10.37	16.07	0.10	*C*
269.65	10.37	14.95	0.03	*C*	3357.94	10.37	15.93	0.07	*C*
298.43	10.37	14.89	0.04	*C*	3387.40	10.37	16.02	0.07	*C*
327.97	10.37	14.94	0.03	*C*	3416.17	10.37	15.85	0.07	*C*
356.66	10.37	15.02	0.04	*C*	3445.03	10.37	16.32	0.12	*C*
385.86	10.37	15.00	0.03	*C*	3473.80	10.37	15.87	0.06	*C*
415.24	10.37	15.06	0.04	*C*	3488.31	139.97	15.91	0.03	*C*
444.70	10.37	15.12	0.03	*C*	3502.48	10.37	16.25	0.08	*C*
473.73	10.37	15.12	0.04	*C*	3531.77	10.37	15.75	0.06	*C*
502.85	10.37	15.17	0.04	*C*	3561.06	10.37	15.77	0.07	*C*
531.53	10.37	15.20	0.04	*C*	3618.69	10.37	16.05	0.09	*C*
561.08	10.37	15.38	0.05	*C*	3647.64	10.37	15.84	0.09	*C*
589.85	10.37	15.34	0.04	*C*	3676.67	10.37	16.00	0.10	*C*
618.54	10.37	15.42	0.04	*C*	3705.44	10.37	16.09	0.09	*C*
648.09	10.37	15.26	0.05	*C*	3785.36	147.74	16.13	0.05	*C*
677.29	10.37	15.46	0.05	*C*	3796.07	10.37	16.00	0.11	*C*
705.97	10.37	15.45	0.03	*C*	3827.87	10.37	15.97	0.09	*C*
734.75	10.37	15.44	0.04	*C*	3859.49	10.37	16.24	0.11	*C*
763.86	10.37	15.40	0.04	*C*	3891.54	10.37	16.40	0.15	*C*
793.33	10.37	15.75	0.09	*C*	3923.08	10.37	16.07	0.10	*C*
850.87	10.37	15.65	0.04	*C*	3954.87	10.37	16.24	0.11	*C*
865.47	140.83	15.62	0.02	*C*	3986.58	10.37	16.39	0.09	*C*
879.90	10.37	15.65	0.05	*C*	4018.03	10.37	16.29	0.09	*C*
908.84	10.37	15.50	0.04	*C*	4050.26	10.37	15.74	0.07	*C*
937.87	10.37	15.69	0.05	*C*	4081.88	10.37	15.85	0.06	*C*
966.99	10.37	15.82	0.08	*C*	4098.04	152.93	16.03	0.04	*C*
996.19	10.37	15.80	0.04	*C*	4113.76	10.37	16.07	0.10	*C*
1025.48	10.37	15.71	0.04	*C*	4145.39	10.37	16.11	0.11	*C*
1054.25	10.37	15.75	0.05	*C*	4177.35	10.37	15.93	0.09	*C*
1083.46	10.37	15.80	0.05	*C*	4209.06	10.37	15.89	0.10	*C*
1112.23	10.37	15.73	0.04	*C*	4241.29	10.37	16.41	0.14	*C*
1141.17	10.37	15.70	0.04	*C*	4273.43	10.37	15.82	0.08	*C*
1155.77	139.97	15.80	0.02	*C*	4305.23	10.37	15.96	0.08	*C*
1170.29	10.37	15.90	0.09	*C*	4337.45	10.37	15.85	0.08	*C*
1198.97	10.37	16.05	0.07	*C*	4369.25	10.37	15.81	0.07	*C*
1228.35	10.37	15.80	0.05	*C*	4400.96	10.37	15.65	0.05	*C*
1257.29	10.37	15.89	0.06	*C*	4417.29	153.79	15.81	0.03	*C*
1286.06	10.37	15.78	0.08	*C*	4433.36	10.37	15.69	0.09	*C*
1314.75	10.37	16.00	0.08	*C*	4465.07	10.37	15.51	0.07	*C*
1344.04	10.37	16.14	0.10	*C*	4497.12	10.37	16.26	0.12	*C*
1373.16	10.37	16.07	0.06	*C*	4529.00	10.37	15.78	0.05	*C*
1402.27	10.37	16.13	0.11	*C*	4561.14	10.37	15.78	0.08	*C*
1431.30	10.37	16.13	0.05	*C*	4592.94	10.37	15.83	0.08	*C*
1445.47	140.83	16.06	0.03	*C*	4625.08	10.37	15.93	0.12	*C*
1460.16	10.37	16.13	0.07	*C*	4656.96	10.37	15.82	0.07	*C*
1489.54	10.37	16.07	0.05	*C*	4689.27	10.37	15.95	0.07	*C*
1547.42	10.37	16.16	0.05	*C*	4721.07	10.37	15.97	0.09	*C*
1576.28	10.37	16.14	0.10	*C*	4736.36	153.79	15.82	0.03	*C*
1605.05	10.37	16.38	0.07	*C*	4752.78	10.37	15.92	0.06	*C*
1634.00	10.37	16.26	0.10	*C*	4784.23	10.37	15.73	0.06	*C*
1663.20	10.37	16.24	0.10	*C*	4816.28	10.37	15.78	0.07	*C*
1692.49	10.37	16.32	0.12	*C*	4847.99	10.37	15.80	0.06	*C*
1721.95	10.37	16.44	0.11	*C*	4879.79	10.37	15.85	0.06	*C*
1735.95	140.83	16.25	0.04	*C*	4911.75	10.37	15.70	0.07	*C*
1750.64	10.37	15.91	0.07	*C*	4943.55	10.37	15.71	0.07	*C*

Table 2
(Continued)

$T - T_0$ (s)[a]	Exp. (s)	Mag	1σ[b]	Filter	$T - T_0$ (s)	Exp (s)	1σ[b]	Error	Filter
1779.32	10.37	16.32	0.09	*C*	4975.43	10.37	15.70	0.09	*C*
1837.38	10.37	16.13	0.07	*C*	5007.57	10.37	15.63	0.08	*C*
1866.84	10.37	16.12	0.06	*C*	5039.63	10.37	15.76	0.05	*C*
2198.53	10.37	16.37	0.07	*C*	5055.09	152.93	15.76	0.04	*C*
2227.74	10.37	16.17	0.07	*C*	5071.25	10.37	15.78	0.07	*C*
2257.20	10.37	16.57	0.16	*C*	5102.87	10.37	16.08	0.09	*C*
2285.97	10.37	16.26	0.12	*C*	5135.10	10.37	15.76	0.06	*C*
2314.74	10.37	16.63	0.15	*C*	5166.63	10.37	15.84	0.10	*C*
2329.43	140.83	16.27	0.04	*C*	5198.34	10.37	15.81	0.07	*C*
2343.60	10.37	16.22	0.08	*C*	5230.48	10.37	16.01	0.10	*C*
2372.63	10.37	16.40	0.13	*C*	5262.19	10.37	15.52	0.07	*C*
2401.92	10.37	15.91	0.05	*C*	5262.19	41.47	15.80	0.06	*C*
2431.12	10.37	16.29	0.10	*C*	5293.99	10.37	15.82	0.08	*C*
2460.33	10.37	16.47	0.14	*C*	5524.24	10.37	15.91	0.15	*C*
2489.70	10.37	16.11	0.08	*C*	5696.01	152.93	15.68	0.06	*C*
2518.47	10.37	15.94	0.07	*C*	5774.63	10.37	15.72	0.09	*C*
2547.50	10.37	16.09	0.04	*C*	5839.00	10.37	15.89	0.08	*C*
2576.19	10.37	16.24	0.08	*C*	5870.88	10.37	15.65	0.08	*C*
2604.96	10.37	16.46	0.08	*C*	5967.04	10.37	16.13	0.11	*C*
2619.65	139.97	16.07	0.02	*C*	5998.75	10.37	15.68	0.10	*C*
2633.73	10.37	16.03	0.05	*C*	6015.08	154.66	15.75	0.04	*C*
2662.50	10.37	16.01	0.08	*C*	6063.03	10.37	15.69	0.11	*C*
2691.88	10.37	16.26	0.08	*C*	6127.66	10.37	15.73	0.12	*C*
2720.74	10.37	16.00	0.07	*C*	6318.95	10.37	15.99	0.12	*C*
2749.59	10.37	16.07	0.07	*C*	6335.37	153.79	15.81	0.04	*C*
2778.62	10.37	16.30	0.08	*C*	6383.06	10.37	15.98	0.14	*C*
2807.65	10.37	15.85	0.06	*C*	6415.55	10.37	15.96	0.12	*C*
2836.43	10.37	16.13	0.07	*C*	6511.54	10.37	15.67	0.09	*C*
2865.28	10.37	16.05	0.06	*C*	6543.24	10.37	15.75	0.10	*C*
2894.14	10.37	16.04	0.09	*C*	6638.20	10.37	16.07	0.11	*C*
2908.83	139.97	16.09	0.04	*C*	6654.27	152.93	15.95	0.05	*C*
2923.69	10.37	16.31	0.09	*C*	6669.99	10.37	15.89	0.08	*C*
2952.46	10.37	16.16	0.09	*C*	6701.53	10.37	15.78	0.10	*C*
2981.15	10.37	16.07	0.08	*C*	6733.58	10.37	16.21	0.13	*C*
3010.26	10.37	15.99	0.06	*C*	6797.00	10.37	16.10	0.14	*C*
3039.03	10.37	16.14	0.07	*C*	…	…	…	…	…
				TNT					
34,185.0	300.00	18.31	0.11	*R*	37,368.0	300.00	18.48	0.09	*R*
34,824.0	300.00	18.33	0.07	*R*	38,005.0	300.00	18.67	0.09	*R*
35,460.0	300.00	18.58	0.09	*R*	107,777.0	1800.00	20.56	0.13	*R*
36,096.0	300.00	18.66	0.13	*R*	194,435.0	1500.00	>20.39	…	*R*
36,732.0	300.00	18.61	0.09	*R*	368,627.0	2850.00	>20.56	…	*R*
				Lightbuckets					
975.0	30.00	15.74	0.02	*R*	1224.0	30.00	15.93	0.02	*R*
1099.0	30.00	15.84	0.02	*R*	1384.0	30.00	16.01	0.02	*R*
				Celestron C14 XLT					
43,563.0	600.00	18.87	0.11	*C*	45,604.0	600.00	19.07	0.13	*R*
44,185.0	600.00	18.85	0.10	*C*	46,232.0	600.00	19.13	0.12	*R*
44,806.0	600.00	18.90	0.10	*C*	46,919.0	600.00	19.30	0.16	*R*
				GRAS					
1643.0	300.00	16.01	0.03	*C*	3128.0	300.00	16.18	0.10	*R*
2306.0	300.00	16.22	0.05	*C*	…	…	…	…	…
				AZT-33IK					
22,075.2	240.00	18.00	0.06	*R*	25,870.8	240.00	18.13	0.05	*R*
22,451.0	240.00	18.13	0.05	*R*	26,113.5	240.00	18.17	0.04	*R*
22,694.7	240.00	18.09	0.05	*R*	26,357.2	240.00	18.16	0.06	*R*
22,937.5	240.00	18.13	0.05	*R*	26,600.0	240.00	18.14	0.06	*R*
23,180.3	240.00	18.11	0.05	*R*	26,842.8	240.00	18.15	0.06	*R*
23,440.3	240.00	18.14	0.05	*R*	27,096.8	240.00	18.18	0.06	*R*
23,684.0	240.00	18.12	0.05	*R*	27,339.6	240.00	18.18	0.06	*R*
23,926.8	240.00	18.12	0.06	*R*	27,583.2	240.00	18.12	0.06	*R*
24,169.5	240.00	18.11	0.04	*R*	27,923.6	240.00	18.10	0.06	*R*
24,412.3	240.00	18.09	0.04	*R*	28,166.4	240.00	18.22	0.07	*R*
24,656.0	240.00	18.18	0.05	*R*	28,409.2	240.00	18.04	0.08	*R*

Table 2
(Continued)

$T-T_0$ (s)[a]	Exp. (s)	Mag	1σ[b]	Filter	$T-T_0$ (s)	Exp (s)	1σ[b]	Error	Filter
24,898.8	240.00	18.14	0.04	*R*	28,652.8	240.00	18.17	0.08	*R*
25,141.5	240.00	18.14	0.04	*R*	28,895.6	240.00	18.25	0.13	*R*
25,385.2	240.00	18.12	0.04	*R*	198,490.0	3600.00	21.18	0.12	*R*
25,628.0	240.00	18.13	0.04	*R*	…	…	…	…	…
				AZT-11					
139,063.00	3600.00	>19.90	…	*R*	…	…	…	…	…

Notes.
[a] $T-T_0$ is the midpoint of each observation. The reference time T_0 is the Swift/BAT burst trigger time.
[b] 1σ is the uncertainty in the magnitude.

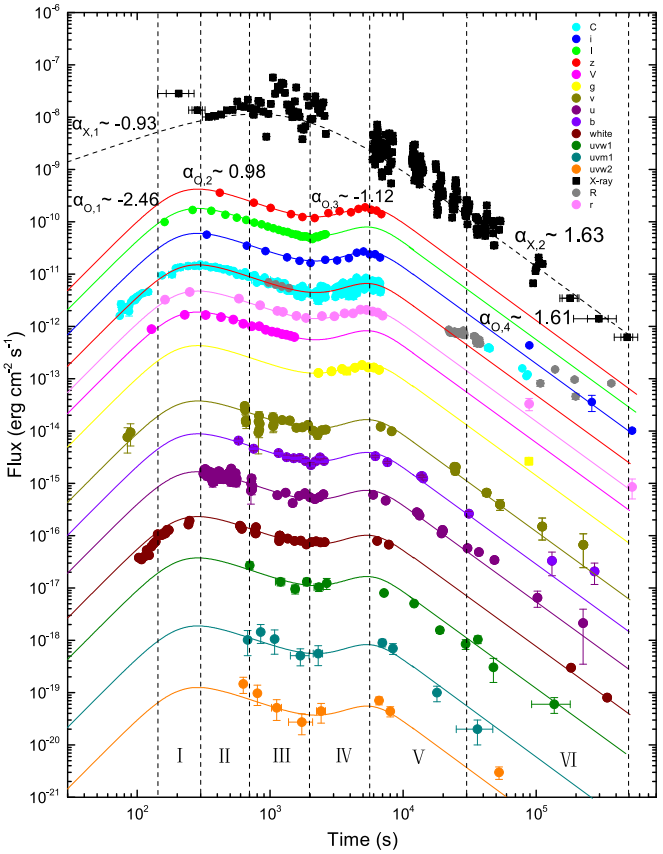

Figure 1. X-ray and 15 optical light curves of GRB 110213A, and our empirical fit with multiple broken-power laws for the multiwavelength afterglow. The vertical dashed lines mark the phases of interest for the afterglow spectral analysis. Some data are taken from Cucchiara et al. (2011).

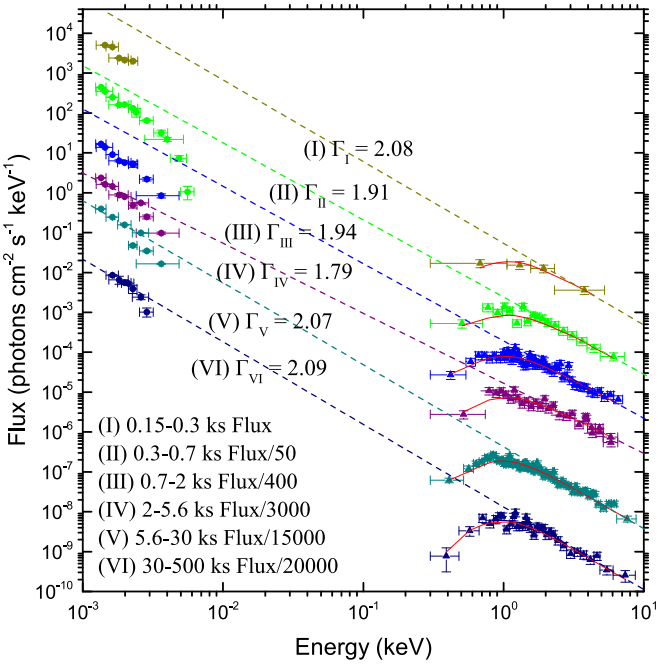

Figure 2. SED analysis of GRB 110213A. The dashed lines show the intrinsic power-law spectra derived from X-ray afterglow. The photon indices are also marked.

Table 3
Spectral Analysis of Afterglow

Phase	Interval (ks)	Γ	χ^2/dof
I	0.15–0.3	2.08 ± 0.24	1.38
II	0.3–7	1.91 ± 0.10	1.65
III	0.7–2	1.94 ± 0.06	1.07
IV	2–6	1.79 ± 0.09	1.19
V	6–30	2.07 ± 0.03	1.44
VI	30–500	2.09 ± 0.08	1.36

in the late-time afterglow (after ~5.6 ks, Phases IV–VI). Cucchiara et al. (2011) presented an energy-injection model to explain the second optical peak, but it cannot sufficiently explain the X-ray emission since no clear X-ray rebrightening was observed at the same phase. Here, we try a different model.

Combining the results of our temporal analysis and spectral analysis, we use the closure relation (α–β) of the fireball external-shock model (e.g., Sari et al. 1998; Zhang et al. 2006; Gao et al. 2013; Wang et al. 2015) to test the late-time afterglow (after ~5.6 ks, Phases IV–VI) of GRB 110213A. Here, β is adopted as the average from the late-time afterglow (Phase IV–VI), with $\beta = \Gamma - 1 \approx 1.1$. The temporal results illustrate that $\Delta\alpha = \alpha_{O,4} - \alpha_{X,2} \approx 0$. Assuming the GRB 110213A multiwavelength data are located in the same spectral regime e.g., $\nu_m < \nu_O < \nu_X < \nu_c$, where ν_m and ν_c are (respectively) the minimum injection frequency and cooling frequency for synchrotron radiation, and ν_O and ν_X are (respectively) the optical frequency and the X-ray frequency; and the circumburst medium is just the interstellar medium (ISM). One can see that the both X-ray and optical band can be satisfied well with the $\alpha_{O,4} \approx \alpha_{X,2} = 3\beta/2 \approx 1.65$.

4. Theoretical Analysis

4.1. Model

In the framework of the standard dynamic evolution forward-shock model for GRB afterglows (Sari et al. 1998; Huang et al. 1999), we employ the electromagnetic cascade emission of the absorbed teraelectronvolt photons introduced by Huang et al. (2021). The afterglow emission is dominated by synchrotron radiation and the SSC process (e.g., Sari et al. 1998; Sari & Esin 2001; Zhang & Mészáros 2001; Gao et al. 2013; Kumar & Zhang 2015). The Klein–Nishina (KN) effect must be included for the high-energy photons in GRB afterglows (Nakar et al. 2009; Wang et al. 2010; Huang et al. 2021). Cucchiara et al. (2011) suggested that the behavior of the GRB 110213A afterglow is consistent with the slow-cooling regime in a homogeneous medium. In this paper, we give the modified electron distribution in the slow-cooling regime, which can be written as (e.g., Nakar et al. 2009; Wang et al. 2010)

$$N(\gamma_e) = \begin{cases} C\gamma_e^{-p}, & \gamma_m < \gamma_e < \gamma_c \\ \dfrac{1 + Y(\gamma_c)}{1 + Y(\gamma_e)} C\gamma_c \gamma_e^{-p-1}, & \gamma_c < \gamma_e. \end{cases} \quad (4)$$

The distribution of the radiating electrons decays as $dN/d\gamma_e \propto \gamma^{-p}$, where γ_e is the electron Lorentz factor and p is the electron spectral index, γ_m is the minimum injection electron Lorentz factor, γ_c is the cooling Lorentz factor, and C is a constant. $Y(\gamma_e)$ is the Compton parameter, which depends on the energy of the electrons γ_e and is given by

$$Y(\gamma_e) = \frac{U_{\rm syn}[\nu < \nu_{\rm KN}(\gamma_e)]}{U_B}, \quad (5)$$

where $\nu_{\rm KN}$ is the photon frequency above which the scattering with electrons of energy γ_e begins to enter the KN scattering phase, $U_{\rm syn}[\nu < \nu_{\rm KN}(\gamma_e)]$ is the synchrotron photon energy density of frequency less than $\nu_{\rm KN}$, and U_B is the energy density of the magnetic field.

For a relativistic astrophysical process, two photons will annihilate when $h\nu_1\, h\nu_2 \geqslant \Gamma^2(m_e c^2)^2$ in the source. Then the secondary $e^{\pm}$ pairs can produce cascade emission via synchrotron radiation and the IC process. If the opacity $\tau_{\gamma\gamma} \gg 1$, these secondary photons cannot escape the source and proceed to the next phase of two-photon annihilation. This process progresses until the opacity of the secondary photons becomes $\tau_{\gamma\gamma} < 1$, at which point the photons can escape from the source. During these processes, the energy of primary SSC high-energy photons will be redistributed to lower-energy photons, increasing their number.

The parameters of our model include the isotropic kinetic energy $E_{\rm K,iso}$, the initial Lorentz factor Γ_0, the fraction of shock energy to electron energy $\epsilon_{\rm e}$, the fraction of shock energy to magnetic field energy $\epsilon_{\rm B}$, the jet opening angle $\theta_{\rm j}$, and the density profile of the circumburst medium $n(r) \propto r^{-k}$. As an example, Figure 3 shows the opacity of a photon (afterglow phase) with an energy of 1 TeV as a function of time. For parameter values $E_{\rm K,iso} = 5.01 \times 10^{53}$ erg, $\Gamma_0 = 120$, $\epsilon_e = 0.25$, $\epsilon_B = 6.5 \times 10^{-4}$, $n = 0.27$ cm^{-3}, $\theta_j = 0.32$ rad and $k = 1.0$, the opacity exceeds 1 for tens to hundreds of seconds; thereafter, it is <1. This result corresponds to Figure 4; the cascade component can well explain the first optical peak.

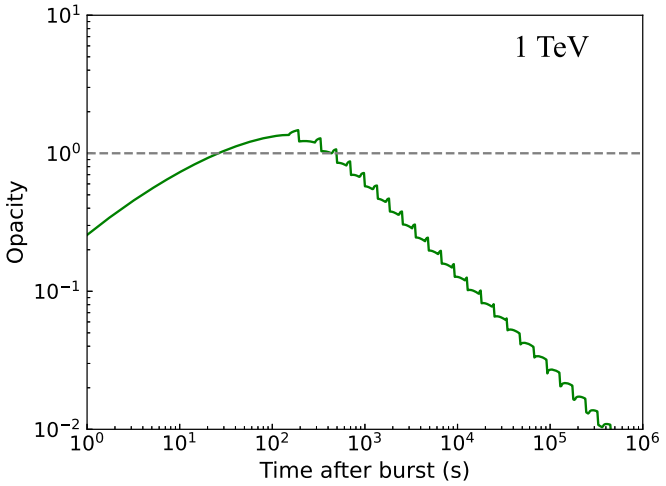

Figure 3. Opacity of photon (afterglow phase) with energy 1 TeV in the source as a function of time. The green line represents the case of our parameters ($E_{\rm K,iso} = 5.01 \times 10^{53}$ erg, $\Gamma_0 = 120$, $\epsilon_e = 0.25$, $\epsilon_B = 6.5 \times 10^{-4}$, $n = 0.27$ cm^{-3}, $\theta_j = 0.32$ rad, and $k = 1.0$). The gray horizontal dashed line represents $\tau_{\gamma\gamma} = 1$.

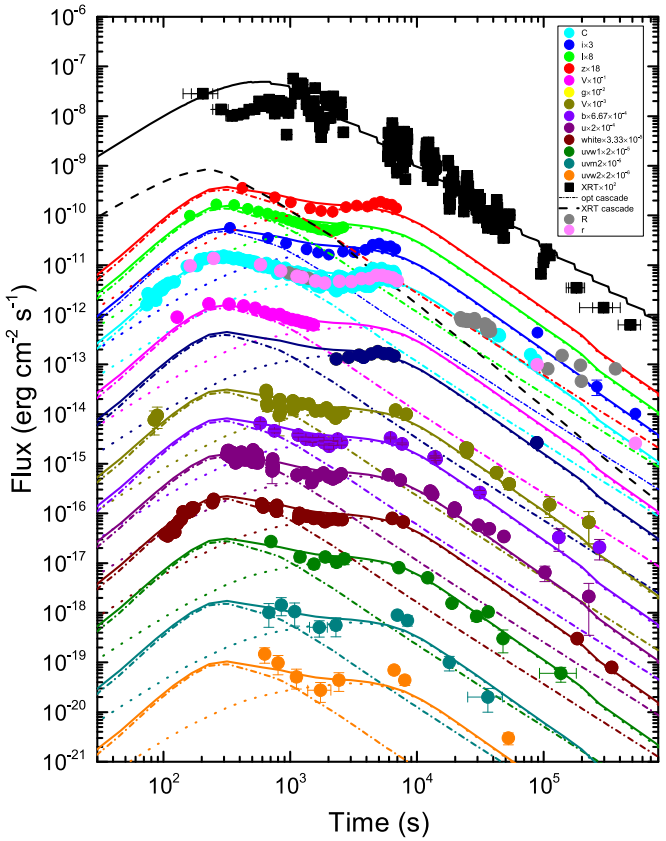

Figure 4. Modeling the multiwavelength light curves with an external-shock model by cascade emission. The synchrotron + SSC and cascade emission are represented with dotted and dotted–dashed lines, respectively. The best-fitting model parameters are $E_{\rm K,iso} = 5.01^{+4.54}_{-3.43} \times 10^{53}$ erg, $\Gamma_0 = 120^{+21}_{-16}$, $\epsilon_e = 0.25^{+0.04}_{-0.05}$, $\epsilon_B = 6.5^{+8.0}_{-2.6} \times 10^{-4}$, $n = 0.27^{+0.19}_{-0.08}$ cm^{-3}, $\theta_j = 0.32^{+0.26}_{-0.20}$ rad, and $k = 1.0^{+0.3}_{-0.3}$.

We adopt an efficient semianalytical method to calculate the cascade radiation (Böttcher et al. 2013; Huang et al. 2021). In addition, we provide a meaningful constraint on the parameters by using the data-fitting code "emcee" (Foreman-Mackey et al. 2013), which is widely used based on Markov chain Monte

Carlo (MCMC) simulations. One can denote the injection rate of first-generation high-energy photons (produced from synchrotron radiation and SSC) as $\dot{N}_\epsilon^0$, production rates of secondary high-energy photons (from synchrotron emission and the IC process) as $\dot{N}_\epsilon^{\rm sec}$, and the optical depth for $\gamma\gamma$ absorption as $\tau_{\gamma\gamma}(\epsilon)$. The spectrum of escaping (observable) photons ($\dot{N}_\epsilon^{\rm esc}$) can then be described as (Böttcher et al. 2013; Huang et al. 2021)

$$\dot{N}_\epsilon^{\rm esc} = (\dot{N}_\epsilon^0 + \dot{N}_\epsilon^{\rm sec})\left(\frac{1 - e^{-\tau_{\gamma\gamma}(\epsilon)}}{\tau_{\gamma\gamma}(\epsilon)}\right). \quad (6)$$

When the opacity $\tau_{\gamma\gamma}(\epsilon) \gg 1$, the photons cannot escape from the source, and the electron/positron pairs are produced due to $\gamma\gamma$ absorption. Assuming the energy of a high-energy photon is ϵ, the produced electron-positron pair has energies $\gamma_1 = f_{\gamma_e}\epsilon$ and $\gamma_2 = (1 - f_{\gamma_e})\epsilon$ (here the major fraction of photon energy is f_{γ_e}). The pair-production rates can be written as (Böttcher et al. 2013; Veres et al. 2017; Huang et al. 2021)

$$\dot{N}_{\rm e}^{\gamma\gamma}(\gamma_e) = f_{\rm abs}(\epsilon_1)(\dot{N}_{\epsilon_1}^0 + \dot{N}_{\epsilon_1}^{\rm sec}) + f_{\rm abs}(\epsilon_2)(\dot{N}_{\epsilon_2}^0 + \dot{N}_{\epsilon_2}^{\rm sec}), \quad (7)$$

where $\epsilon_1 = \gamma_e/f_{\gamma_e}$ and $\epsilon_2 = \gamma_e/(1 - f_{\gamma_e})$. The parameter f_{γ_e} is found to be 0.9 for the cascade problem (Böttcher et al. 2013; Huang et al. 2021). The absorption factor $f_{\rm abs}(\epsilon)$ is defined as

$$f_{\rm abs}(\epsilon) \equiv 1 - \frac{1 - e^{-\tau_{\gamma\gamma}(\epsilon)}}{\tau_{\gamma\gamma}(\epsilon)}. \quad (8)$$

One can calculate the electron energy loss due to synchrotron radiation and the SSC process following (Huang et al. 2021),

$$\dot{\gamma_e} = \frac{4}{3}\frac{c\,\sigma_{\rm T}}{m_e c^2}\gamma_e^2[U_{\rm B} + U_{\rm syn} f_{\rm KN}(\gamma_e)], \quad (9)$$

where m_e is the electron mass, $\sigma_{\rm T}$ is the Thomson scattering cross section, c is the speed of light, and $f_{\rm KN}(\gamma_e)$ is the KN effect correction factor,

$$f_{\rm KN}(\gamma_e) = \int_{\epsilon,\min}^{\epsilon,\max} f_{\rm KN}(\kappa)u(\epsilon)d\epsilon \Big/ U_{\rm syn}, \quad (10)$$

where $u(\epsilon)$ is the energy distribution of the synchrotron photons and $\kappa = 4\gamma_e\epsilon$. When $\kappa \ll 1$ (Thomson limit), we have $f_{\rm KN}(\kappa) \approx 1$, while $f_{\rm KN}(\kappa) \approx (9/2\kappa^2)[\ln\kappa - (11/6)]$ for $\kappa \gg 1$ (KN limit) (Moderski et al. 2005). Note that $\kappa = 1$ corresponds to the transition between the Thomson and KN scattering regimes.

In our emcee (Foreman-Mackey et al. 2013) process, we take time slices in logarithmic space that are sufficiently small [$\delta t = (10^{0.01} - 1)t$] for accurate calculation. When the electron cooling timescale $t_e^{\rm cool}(\gamma_e)$ is less than the time interval δt, the electron distribution can be described as (Huang et al. 2021)

$$N_{\rm e}^{\rm sec}(\gamma_e, t + \delta t) = N_{\rm e}^{\rm sec}(\gamma_e^*, t)\frac{d\gamma_e^*}{d\gamma_e} + \frac{1}{\dot{\gamma}_e}\int_{\gamma_e}^{\infty} d\widetilde{\gamma}_e\, \dot{N}_{\rm e}^{\gamma\gamma}(\widetilde{\gamma}_e, t + \delta t), \quad (11)$$

where γ_e^* is the electron Lorentz factor at time t, and it will decrease to γ_e in time interval δt because of the cooling effect. For another situation, $t_e^{\rm cool}(\gamma_e) > \delta t$, the electron distribution can be described as

$$N_{\rm e}^{\rm sec}(\gamma_e, t + \delta t) = N_{\rm e}^{\rm sec}(\gamma_e^*, t)\frac{d\gamma_e^*}{d\gamma_e} + \dot{N}_{\rm e}^{\gamma\gamma}(\gamma_e, t + \delta t)\,\delta t. \quad (12)$$

4.2. Results

The spectral regimes are assumed to be located in $\nu_{\rm m} < \nu_O < \nu_X < \nu_{\rm c}$ and we fix the electron spectral index $p = 2\beta + 1 = 3.2$. The preliminary parameters are set in the ranges $E_{\rm K,iso} \in [0.01,\ 10^3] \times 10^{53}$ erg, $\Gamma_0 \in [80,\ 180]$, $\epsilon_{\rm e} \in [0.01,\ 0.60]$, $\epsilon_{\rm B} \in [1.0,\ 100.0] \times 10^{-4}$, $n \in [0.01,\ 1.00]$ cm^{-3}, $\theta_j \in [0.01,\ 1.00]$ rad, and $k \in [0,\ 2.0]$.

A set of optimum parameters was obtained through our MCMC, with $E_{\rm K,iso} = 5.01^{+4.54}_{-3.43} \times 10^{53}$ erg, $\Gamma_0 = 120^{+21}_{-16}$, $\epsilon_e = 0.25^{+0.04}_{-0.05}$, $\epsilon_B = 6.5^{+8.0}_{-2.6} \times 10^{-4}$, $n = 0.27^{+0.19}_{-0.08}$ cm^{-3}, $\theta_j = 0.32^{+0.26}_{-0.20}$ rad, and $k = 1.0^{+0.3}_{-0.3}$; the fitting results are shown in Figure 4. Figure 5 shows the parameter corner plot of the fitting for GRB 110213A. The fitting parameters are consistent with the statistical properties of a large sample of GRBs (e.g., Wang et al. 2015). Since we cannot strictly constrain the jet opening angle through the jet-break feature, the lower limit $\theta_{\rm j} \geqslant 0.32$ rad is given.

We find that the chromatic light curve between the X-ray and optical bands can be well described by including a cascade emission. To investigate how the cascade emission contributes to the afterglow of GRB 110213A, we illustrate the broadband SEDs of the afterglows in the early stages ($t = 100$, 300, and 1000 s) and late stages ($t = 10$ hr) with the best-fitting parameters $E_{\rm K,iso} = 5.01 \times 10^{53}$ erg, $\Gamma_0 = 120$, $\epsilon_e = 0.25$, $\epsilon_B = 6.5 \times 10^{-4}$, $n = 0.27$ cm^{-3}, $\theta_j = 0.32$ rad, and $k = 1.0$. As shown in Figure 6, the cascade emission converts teraelectronvolt photons to optical ($\sim$1 eV) photons efficiently, rather than the X-ray photons ($\sim$1 keV). One can see that the optical band is dominated by the cascade emission from synchrotron radiation at early phases, while the primary synchrotron + SSC radiation dominates the X-ray band. For the late stage, both the X-ray and optical bands are dominated by the emission from primary synchrotron + SSC radiation. The combined effects are shown in the light curves of GRB 110213A (as shown in Figure 4). The cascade component can well explain the first optical peak, while the primary synchrotron + SSC emission mainly contributes to the second one.

The GRB radiative efficiency, defined (Lloyd-Ronning & Zhang 2004) as $\eta_\gamma = E_{\gamma,\rm iso}/(E_{\gamma,\rm iso} + E_{\rm K,iso})$, is an essential parameter to probe how efficiently a burst converts its global energy to prompt gamma-ray emission. The $E_{\gamma,\rm iso}$ of GRB 110213A is $7.2^{+0.1}_{-0.08} \times 10^{52}$ erg at $z = 1.46$ (Cucchiara et al. 2011). We find that the value of η_γ for GRB 110213A is $12.6^{+9.6}_{-5.5}$%, consistent with previous results (Zhang et al. 2007; Wang et al. 2015; Zhong et al. 2016).

5. Conclusion and Discussion

We report our well-sampled optical photometric observations of the afterglow of GRB 110213A, and we investigate the physical origins of both the optical and X-ray afterglows.

Combining our data with those from the other ground-based telescopes (Cucchiara et al. 2011), we present 15 optical multiband light curves. They exhibit similar shapes with two

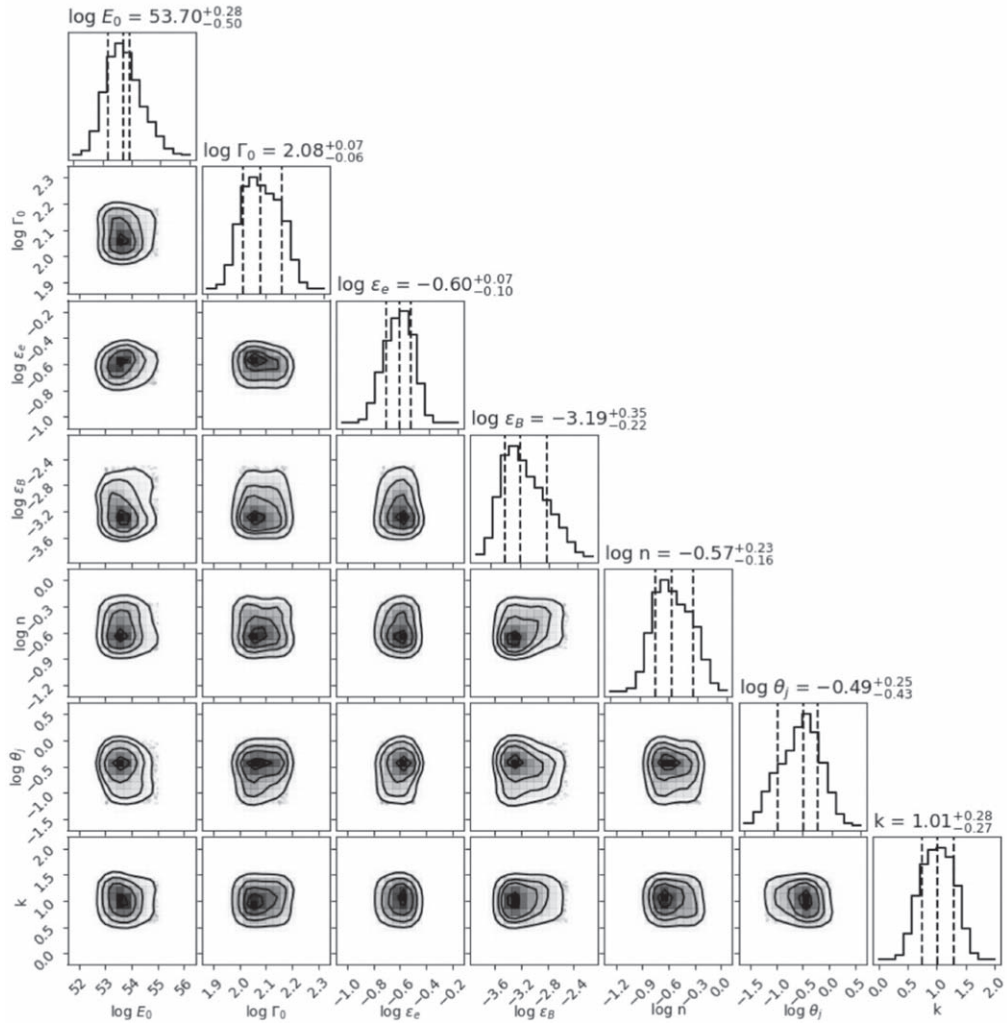

Figure 5. Corner plot showing the results of our MCMC parameter estimation with an external shock and cascade emission model, and histograms on the diagonal showing the marginalized posterior densities for each parameter. A two-dimensional projection of the sample is plotted to reveal covariances. The uncertainties are computed as the 16th and 84th percentiles of the posterior samples along each axis, thus representing 1σ confidence ranges shown with black dashed vertical lines. Our best-fit parameters are also indicated with black dashed vertical lines.

bumps (one peaking at ∼213 s, the other at ∼5.6 ks). In the X-ray band, however, only one bump is seen; its peak (at ∼1.4 ks) is between the two optical peaks; thus, the optical and X-ray light curves exhibit chromatic behavior before ∼5.6 ks. Thereafter, the X-ray and optical multiband light curves have the same temporal behavior. Also, our analysis shows that the X-ray spectrum differs from the optical band for Phases I–III (before the second optical peak, ∼5.6 ks). They have the same spectral behavior in the late afterglow phase (after ∼5.6 ks; Phases IV–VI). This indicates that the optical and X-ray emission have a different origin.

Synchrotron-supported pair cascade emission is included in the standard external forward-shock model, which is dominated by synchrotron radiation and SSC. We find that the chromatic light curve between the X-ray and optical bands of GRB 110213A can be well described by including cascade emission. The best-fitting parameters are $E_{\rm K,iso} = 5.01^{+4.54}_{-3.43} \times 10^{53}$ erg, $\Gamma_0 = 120^{+21}_{-16}$, $\epsilon_e = 0.25^{+0.04}_{-0.05}$, $\epsilon_B = 6.5^{+8.0}_{-2.6} \times 10^{-4}$, $n = 0.27^{+0.19}_{-0.08}$ cm^{-3}, $\theta_j = 0.32^{+0.26}_{-0.20}$ rad, and $k = 1.0^{+0.3}_{-0.3}$. The optical band is dominated by the cascade emission from synchrotron radiation during the early phases, while primary synchrotron + SSC radiation dominate the X-ray band. At late times, both the X-ray and optical bands are dominated by emission from primary synchrotron + SSC radiation. The cascade component can explain the first optical bump, while the primary synchrotron + SSC emission mainly contribute to the second one.

One notices that for the UVOT-*white* band (shown as green filled dots), the rising index is steeper ($\alpha = 3.28 \pm 0.40$ if fit only to the UVOT-*white* data) than the fitting value for the *R* band ($\alpha \approx 2.44$). This is also the main cause of the large χ^2 fitting residual compared with other UVOT filters (see Table 1). Since the UVOT-*white* band (equivalent $\lambda = 3471$ Å) covers a much bluer region than *R* (equivalent $\lambda = 6407$ Å), we speculate that the steeper rise may be caused by a decreasing extinction with time near the GRB. Although little clear observational evidence of changing extinction has been previously found in GRBs, theoretical models suggest that dust can be destroyed by strong GRB X-ray and UV flashes along our line of sight, so a time-variable extinction is not impossible (e.g., Liang & Kargatis 1994; Perna & Loeb 1998; Böttcher et al. 1999; Waxman & Draine 2000; Fruchter et al. 2001; Lazzati et al. 2002; De Pasquale et al. 2003). Another well-observed object, GRB 110205A, also shows a steeper rise

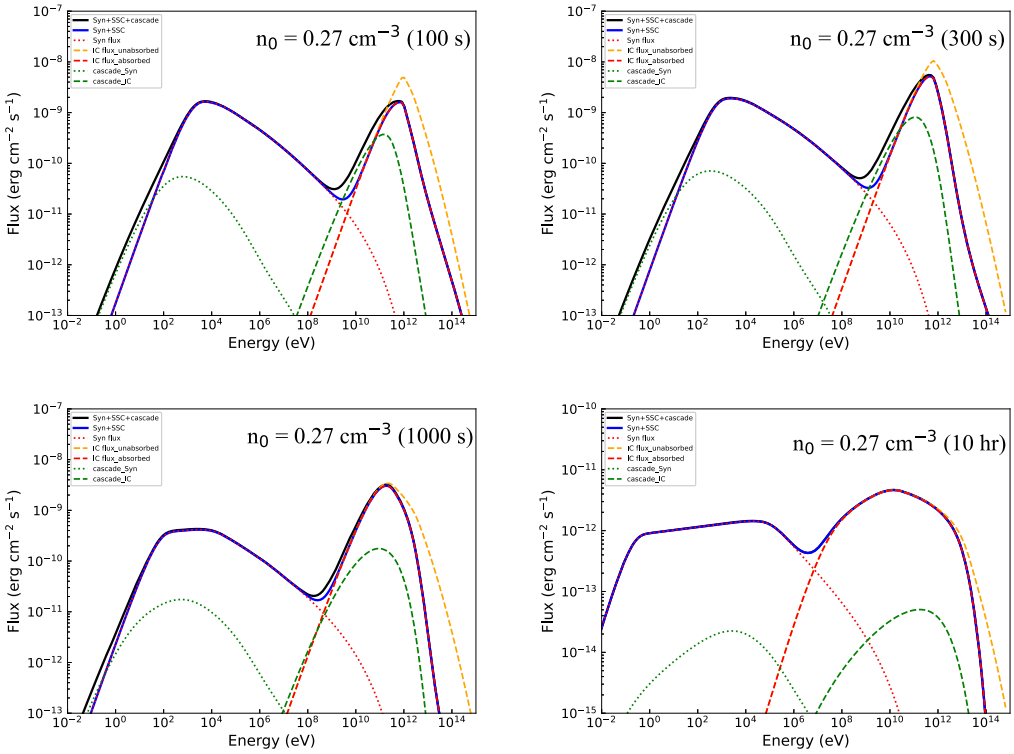

Figure 6. Broadband SEDs of GRB afterglows at early times ($t = 100$, 300, and 1000 s after the trigger) and at a late time ($t = 10$ hr after the trigger). Other parameter values used are $E_{\rm K,iso} = 5.01 \times 10^{53}$ erg, $\Gamma_0 = 120$, $\epsilon_e = 0.25$, $\epsilon_B = 6.5 \times 10^{-4}$, $n = 0.27$ cm^{-3}, $\theta_j = 0.32$ rad, and $k = 1.0$. The yellow dashed lines represent the emission from the SSC process without considering absorption in the source. The solid lines represent the sum of the emission from the synchrotron radiation (dotted lines) and the absorbed radiation of the SSC component (dashed lines).

in the UVOT u band ($\alpha \approx 6$) than in the R band ($\alpha \approx 5$). With more than one observed case of this phenomenon, time-variable extinction may exist in a certain fraction (likely to be very small) of all GRBs. Early-time UV observations (e.g., with UVOT) are essential for exploring this question in more detail.

Huang et al. (2021) found that the cascade emission in the homogeneous circumburst ISM can be comparable to the synchrotron emission of the primary electrons in the optical band and flattens the early-time optical afterglow light curve, when $n \geqslant 1$ cm^{-3}. In contrast, in the wind circumburst medium, the cascade emission at early times is comparable to or even larger than the emission of the primary electrons over a wide range of frequencies. Our result for the density profile, $k \approx 1$, is between the wind ($k = 2$; e.g., Dai & Lu 1998; Vink et al. 2000; Dai & Wu 2003; Chevalier et al. 2004; Vink & de Koter 2005; Xin et al. 2012) and ISM cases ($k = 0$; e.g., Panaitescu 2002). The value of k for GRB 110213A is also consistent with that from large-sample analyses (Liang et al. 2013; Yi et al. 2013; Huang et al. 2018; Li et al. 2020; Xie et al. 2020), suggesting that the density profile may be diverse. The superimposed effect of emission from both the primary and cascade electrons may result in diverse GRB afterglow light curves. Wang et al. (2015) found that 37 of 85 GRBs are also consistent with having an achromatic break, even though one or more afterglow segments do not comply with the external forward-shock closure relations. When more advanced modeling (e.g., long-lasting reverse shock, structured jets, arbitrary circumburst medium density profile) is invoked, up to >90% of afterglows may be interpreted within the framework of the external-shock models. Cascade emission may help us understand the more complicated afterglows of GRBs.

We thank the anonymous referee for their valuable comments and suggestions. This research used public data from the Swift data archive and the UK Swift Science Data Center. This work is supported by the National Natural Science Foundation of China (grants U1938201, 12133003, 12203015, 12103055, 11863007, 11973055, 11903019, 11833003, and 12041306), the Guangxi Science Foundation (grant 2018GXNSFGA281007), and the Innovation Project of Guangxi Graduate Education (grant YSCW2019050). A.V.F. 's group at U.C. Berkeley has been supported by the Christopher R. Redlich Fund and many other individual donors.

ORCID iDs

Xiang-Gao Wang https://orcid.org/0000-0001-8411-8011
WeiKang Zheng https://orcid.org/0000-0002-2636-6508
Valerio D'Elia https://orcid.org/0000-0002-7320-5862
Tilan Ukwatta https://orcid.org/0000-0002-4989-8662
Jin-Jun Geng https://orcid.org/0000-0001-9648-7295
Xu-Hui Han https://orcid.org/0000-0002-6107-0147
N. Paul M. Kuin https://orcid.org/0000-0003-4650-4186
B. E. Schaefer https://orcid.org/0000-0002-2659-8763
Xue-Feng Wu https://orcid.org/0000-0002-6299-1263
En-Wei Liang https://orcid.org/0000-0002-7044-733X
Bing Zhang https://orcid.org/0000-0002-9725-2524
Alexei V. Filippenko https://orcid.org/0000-0003-3460-0103

References

Aharonian, F. A., Khangulyan, D., & Costamante, L. 2008, MNRAS, 387, 1206

Atwood, W. B., Abdo, A. A., Ackermann, M., et al. 2009, ApJ, 697, 1071
Barthelmy, S. D., Cannizzo, J. K., Gehrels, N., et al. 2005, ApJL, 635, L133
Böttcher, M., Dermer, C. D., Crider, A. W., et al. 1999, A&A, 343, 111
Böttcher, M., Reimer, A., Sweeney, K., et al. 2013, ApJ, 768, 54
Breeveld, A. A., Curran, P. A., Hoversten, E. A., et al. 2010, MNRAS, 406, 1687
Breeveld, A. A., Landsman, W., Holland, S. T., et al. 2011, , in AIP Conf. Proc. 1358, Gamma Ray Bursts (Melville, NY: AIP), 373
Burrows, D. N., Hill, J. E., Nousek, J. A., et al. 2005, SSRv, 120, 165
Chevalier, R. A., Li, Z.-Y., & Fransson, C. 2004, ApJ, 606, 369
Chincarini, G., Moretti, A., Romano, P., et al. 2007, ApJ, 671, 1903
Cucchiara, A., Cenko, S., Bloom, J., et al. 2011, ApJ, 743, 154
Dai, Z., Daigne, F., & Mészáros, P. 2017, SSRv, 212, 409
Dai, Z. G., & Lu, T. 1998, A&A, 333, L87
Dai, Z. G., & Wu, X. F. 2003, ApJL, 591, L21
De Pasquale, M., Kuin, N. P. M., Oates, S., et al. 2015, MNRAS, 449, 1024
De Pasquale, M., Oates, S. R., Racusin, J. L., et al. 2016, MNRAS, 455, 1027
De Pasquale, M., Piro, L., Perna, R., et al. 2003, ApJ, 592, 1018
Du, M., Yi, S.-X., Liu, T., et al. 2021, ApJ, 908, 242
Evans, P. A., Beardmore, A. P., Page, K. L., et al. 2007, A&A, 469, 379
Evans, P. A., Beardmore, A. P., Page, K. L., et al. 2009, MNRAS, 397, 1177
Evans, P. A., Willingale, R., Osborne, J. P., et al. 2010, A&A, 519, 102
Fan, Y., & Piran, T. 2006, MNRAS, 369, 197
Fan, Y. Z., & Wei, D. M. 2005, MNRAS, 364, L42
Foreman-Mackey, D., Hogg, D. W., Lang, D., & Goodman, J. 2013, PASP, 125, 306
Fruchter, A., Krolik, J. H., & Rhoads, J. E. 2001, ApJ, 563, 597
Gao, H., Lei, W.-H., Zou, Y.-C., Wu, X.-F., & Zhang, B. 2013, NewAR, 57, 141
Gehrels, N., Chincarini, G., Giommi, P., et al. 2004, ApJ, 611, 1005
Gill, R., & Granot, J. 2018, MNRAS, 475, L1
Golenetskii, S., Aptekar, R., Frederiks, D., et al. 2011, GCN Circ, 11723, 1
Greiner, J., Krühler, T., Nardini, M., et al. 2013, A&A, 560, A70
Hentunen, V. P., Nissinen, M., & Salmi, T. 2011a, GCN Circ, 11709, 1
Hentunen, V. P., Nissinen, M., Salmi, T., & Vilokki, H. 2011b, GCN Circ, 11717, 1
Hou, S. J., Geng, J. J., Wang, K., et al. 2014, ApJ, 785, 113
Huang, K. Y., Urata, Y., Kuo, P. H., et al. 2007, ApJL, 654, L25
Huang, L.-Y., Wang, X.-G., Zheng, W., et al. 2018, ApJ, 859, 163
Huang, X.-L., Wang, Z.-R., Liu, R.-Y., et al. 2021, ApJ, 908, 225
Huang, Y. F., Dai, Z. G., & Lu, T. 1999, MNRAS, 309, 513
Ioka, K., Kobayashi, S., & Zhang, B. 2005, ApJ, 631, 429
Kann, D. A., Klose, S., & Zeh, A. 2006, ApJ, 641, 993
Kann, D. A., Klose, S., Zhang, B., et al. 2010, ApJ, 720, 1513
Kann, D. A., Klose, S., Zhang, B., et al. 2011, ApJ, 734, 96
Kumar, P., Narayan, R., & Johnson, J. L. 2008, MNRAS, 388, 1729
Kumar, P., & Zhang, B. 2015, PhR, 561, 1
Laskar, T., Berger, E., Margutti, R., et al. 2015, ApJ, 814, 1
Lazzati, D., & Perna, R. 2007, MNRAS, 375, L46
Lazzati, D., et al. 2002, MNRAS, 330, 583
Li, L., Liang, E.-W., Tang, Q.-W., et al. 2012, ApJ, 758, 27
Li, W., Filippenko, A. V., Chornock, R., & Jha, S. 2003, PASP, 115, 844
Li, X.-Q., Wen, X.-A., An, Z.-H., et al. 2020, SSPMA, 50, 129508
Liang, E.-W., Yi, S.-X., Zhang, J., et al. 2010, ApJ, 725, 2209
Liang, E. P., & Kargatis, V. E. 1994, ApJL, 432, L111
Liang, E.-W., Li, L., Gao, H., et al. 2013, ApJ, 774, 13
Liang, E.-W., Racusin, J. L., Zhang, B., et al. 2008, ApJ, 675, 528
Liang, E.-W., Zhang, B., O'Brien, P. T., et al. 2006, ApJ, 646, 351
Liang, E.-W., Zhang, B.-B., & Zhang, B. 2007, ApJ, 670, 565
Lloyd-Ronning, N. M., & Zhang, B. 2004, ApJ, 613, 477
Margutti, R., Guidorzi, C., Chincarini, G., et al. 2010, MNRAS, 406, 2149
Maselli, A., Melandri, A., Nava, L., et al. 2014, Sci, 343, 48
Maxham, A., & Zhang, B. 2009, ApJ, 707, 1623
Meegan, C., Lichti, G., Bhat, P. N., et al. 2009, ApJ, 702, 791
Melandri, A., Virgili, F. J., Guidorzi, C., et al. 2014, A&A, 572, A55
Mészáros, P. 2002, ARA&A, 40, 137
Meszaros, P., & Rees, M. J. 1993, ApJ, 405, 278
Mészáros, P., & Rees, M. J. 1997, ApJ, 476, 232
Milne, P. A., & Cenko, S. B. 2011, GCN Circ, 11708, 1
Moderski, R., Sikora, M., Coppi, P. S., et al. 2005, MNRAS, 363, 954
Nakar, E., Ando, S., & Sari, R. 2009, ApJ, 703, 675
Nardini, M., Ghisellini, G., Ghirlanda, G., et al. 2006, A&A, 451, 821
Nardini, M., Greiner, J., Krühler, T., et al. 2011, A&A, 531, A39
Nousek, J. A., Kouveliotou, C., Grupe, D., et al. 2006, ApJ, 642, 389
Panaitescu, A., & Kumar, P. 2002, ApJ, 571, 779
Panaitescu, A., Mészáros, P., Burrows, D., et al. 2006, MNRAS, 369, 2059
Panaitescu, A., & Vestrand, W. T. 2008, MNRAS, 387, 497
Panaitescu, A., & Vestrand, W. T. 2011, MNRAS, 414, 3537
Pe'er, A., & Waxman, E. 2005, ApJ, 628, 857
Perley, D. A., Cenko, S. B., Corsi, A., et al. 2014, ApJ, 781, 37
Perna, R., & Loeb, A. 1998, ApJ, 501, 467
Piran, T. 2004, RvMP, 76, 1143
Poole, T. S., Breeveld, A. A., Page, M. J., et al. 2008, MNRAS, 383, 627
Quimby, R. M., Rykoff, E. S., Yost, S. A., et al. 2006, ApJ, 640, 402
Racusin, J. L., Liang, E. W., Burrows, D. N., et al. 2009, ApJ, 698, 43
Rees, M. J., & Meszaros, P. 1994, ApJL, 430, L93
Roming, P. W. A., Kennedy, T. E., Mason, K. O., et al. 2005, SSRv, 120, 95
Rujopakarn, W., Schaefer, B., & Rykoff, E. 2011, GCN Circ. 11707
Rumyantsev, V., Antoniuk, K., & Pozanenko, A. 2011, GCN Circ. 11744, 11744, 1
Rykoff, E. S., Aharonian, F., Akerlof, C. W., et al. 2009, ApJ, 702, 489
Sari, R., & Esin, A. A. 2001, ApJ, 548, 787
Sari, R., Piran, T., & Narayan, R. 1998, ApJL, 497, L17
Schlegel, D. J., Finkbeiner, D. P., & Davis, M. 1998, ApJ, 500, 525
Tagliaferri, G., Goad, M., Chincarini, G., et al. 2005, Natur, 436, 985
Ukwatta, T., Sonbas, E., Gehrels, N., et al. 2011, GCN Circ, 11715, 1
Veres, P., Dermer, C. D., & Dhuga, K. S. 2017, ApJ, 847, 39
Vink, J. S., & de Koter, A. 2005, A&A, 442, 587
Vink, J. S., de Koter, A., & Lamers, H. J. G. L. M. 2000, A&A, 362, 295
Volnova, A., Pozanenko, A., Korobtsev, I., et al. 2011, GCN Circ, 11742, 1
Wang, X.-G., Zhang, B., Liang, E.-W., et al. 2015, ApJS, 219, 9
Wang, X.-G., Zhang, B., Liang, E.-W., et al. 2018, ApJ, 859, 160
Wang, X.-Y., He, H.-N., Li, Z., et al. 2010, ApJ, 712, 1232
Warren, D. C., Ellison, D. C., Barkov, M. V., & Nagataki, S. 2017, ApJ, 835, 248
Waxman, E., & Draine, B. T. 2000, ApJ, 537, 796
Xie, L., Wang, X.-G., Zheng, W., et al. 2020, ApJ, 896, 4
Xin, L. P., Deng, J. S., Zheng, W. K., et al. 2010, ScChG, 53, 56
Xin, L. P., Pozanenko, A., Kann, D. A., et al. 2012, MNRAS, 422, 2044
Xin, L. P., Qiu, Y. L., Wei, J. Y., et al. 2011, GCN Circ. 11731, 11731, 1
Yan, D., & Zhang, L. 2015, MNRAS, 447, 2810
Yi, S.-X., Wu, X.-F., & Dai, Z.-G. 2013, ApJ, 776, 120
Zacharopoulou, O., Khangulyan, D., Aharonian, F. A., et al. 2011, ApJ, 738, 157
Zhang, B., Fan, Y. Z., Dyks, J., et al. 2006, ApJ, 642, 354
Zhang, B., & Mészáros, P. 2001, ApJL, 552, L35
Zhang, B., & Mészáros, P. 2004, IJMPA, 19, 2385
Zhang, B., Zhang, B.-B., Liang, E.-W., et al. 2007, ApJL, 655, L25
Zhang, B. 2018, The Physics of Gamma-Ray Bursts (London: Cambridge Univ. Press)
Zhang, S.-N., Li, T., Lu, F., et al. 2020, SCPMA, 63, 249502
Zheng, W., Deng, J., Zhai, M., et al. 2008, ChJAA, 8, 693
Zhong, S.-Q., Xin, L.-P., Liang, E.-W., et al. 2016, ApJ, 831, 5